PHYSICAL REVIEW A, VOLUME 63, 023816

Three-dimensional model for vectorial fields in vertical-cavity surface-emitting lasers

G. P. Bava, P. Debernardi, and L. Fratta
Dipartimento di Elettronica, Istituto de Ricerca sull'Ingegneria delle Telecomunicazioni e dell' Informazione, Politecnico di Torino,
Istituto Nazionale per la Fisica della Materia, Unita' di Ricerca di Torino, Corso Duca degli Abruzzi, 24, 10129 Torino, Italy

(Received 16 May 2000; published 18 January 2001)

The electromagnetic problem of modeling vertical-cavity surface-emitting lasers with their full three-dimensional characteristics is analyzed, including oxide confinement, mesa mirrors, metal contacts, and noncircular geometries. The model is based on the mode expansion of the electromagnetic field in the continuous basis of cylindrical TE and TM modes of the cavity medium and on coupled mode theory. The full vectorial treatment of the problem allows a correct analysis of the polarization characteristics of these lasers, which is a topic of great interest both for the device physics and for many applications. A comparison between the fully vectorial treatment and the LP scalar approximation is carried out and polarization resolved results for rectangular and elliptical structures are presented.

DOI: 10.1103/PhysRevA.63.023816 PACS number(s): 42.55.Px, 42.55.Sa, 42.25.Ja, 42.25.Lc

I. INTRODUCTION

Vertical-cavity surface-emitting laser (VCSEL) devices are very attractive light sources due to many of their characteristics such as good optical beams, array capabilities, high modulation rates, and low costs; the introduction of an oxide window has also led to lower threshold currents and higher efficiencies [1,2]. In order to achieve even lower thresholds and a monomode operation the trend is to progressively reduce the transverse dimensions of the active region down to the order of the laser wavelength. In these conditions, due to the complexity and reduced dimensions of the devices, scalar approaches [3–5] are not always suitable to treat real VCSEL structures and should be validated by vectorial models that account for their complete three-dimensional (3D) properties.

In any case a vectorial approach is necessary to analyze the polarization properties of VCSEL's which are very important both for a better understanding of the basic physics and from the point of view of the applications, where often a well-defined polarization is required (sensors, communication systems). In this sense, due to their circular symmetric geometry, VCSEL's present a unique opportunity to study the physical mechanisms of polarization selection, for instance with reference to the San Miguel model [6], and to design lasers with the possibility of polarization control [7]. A lot of work has been done in the last years on this topic [6–14] but, generally, modal dichroism and birefringence are taken as parameters in the different models and the quantitative effect of the various involved phenomena is still not completely analyzed. A theoretical description that not only preserves the full vectorial character of the electromagnetic field but that is also suitable to include the effects of the material anisotropy and of the geometrical asymmetries is therefore needed. Moreover, for small devices, the polarization of the lasing field is no longer perfectly linear and a spatially inhomogeneous polarization has been recently observed as an inherent characteristic of VCSEL's due to their transverse confinement [15]. This effect is common also to gas lasers [16] and its understanding requires a full vectorial electromagnetic treatment of the problem.

Different numerical techniques have up to now been developed to compute the laser modes in VCSEL's. The vectorial problem has been faced with different methods that, generally speaking, can be divided in two main classes: direct numerical solution of Maxwell equations and mode expansion techniques. The former class, which includes the finite elements [17] and weighted index [18] methods or finite-difference time-domain methods [19], suffers from at least two problems: the high computer power required and, related to this, the computation of cold cavity modes; moreover, if at any extent the complexity is lowered, the models can handle only circularly symmetric geometries. In [18] a higher numerical efficiency is acquired by applying a separation of longitudinal and transverse variables in the refractive indexes but this approximation is not valid for complex structures since it leads to constant transverse field profiles. On the other hand, the transform matrix approach proposed in [20] and the modal matrix theory developed in [21] are based on mode expansion of the fields, in terms of the proper modes of a waveguide in the different layers of the stack. In [20] only the circular case is considered, while [21] is applied also to square shapes, but only for the computation of the reflection spectra in a passive case. A self-consistent calculation of the lasing eigenmodes in dielectrically apertured lasers with an active cavity has been performed in [22] where the oxide aperture and the gain profile, are introduced in an idealized way as real and imaginary parts of the complex susceptibility that defines a thin current sheet in the cavity center. If this assumption can well fit the perturbation induced by the quantum well (QW), it is instead very limiting to describe the influence of the oxide diaphragm since information is lost on its thickness and position. Recently, a detailed study on the optimized modal performance of oxide-apertured VCSEL's, related to thickness and position of the oxide window, was performed by [23,24], where the vectorial solution of Maxwell equations is expanded on the discrete set of modes of the structure embedded in a metallic cylinder. In this work we present a comprehensive model to compute the VCSEL modes in complex structures, which has the advantages of both simple analytical derivation and affordability on a PC-level computer power. It is based on the mode expansion of the vectorial electromagnetic field in terms of the continuous basis of the unperturbed cavity modes and all the deviations with respect to the reference unperturbed structure are accounted for by coupled-mode theory. This allows us to put into relation the field in two arbitrary sections of the device and the closure of the problem is obtained by introducing the appropriate boundary conditions of self-consistency between backward and forward waves at two particular sections. In this way, the electromagnetic problem is reduced to an eigenvalue problem where eigenvalues are related to the threshold gain and lasing frequency of the modes, while the corresponding eigenvectors allow the reconstruction of the field profiles. Moreover, the optical response of the QW active material is computed and self-consistency with the solutions of the electromagnetic problem is provided.

The paper is organized as follows. In Sec. II the theoretical model is developed. The adopted mode expansion, coupled-mode formulation, and the boundary conditions are presented. Self-consistency with the material optical response and far-field expressions are reported and a comparison between the fully vectorial treatment and the linearly polarized (LP) scalar approximation is carried out. In Sec. III some examples of numerical results are given. In particular, a parametric study of the laser threshold properties as functions of the device construction characteristics is reported and the influence of the cavity asymmetry on the birefringent behavior is discussed. Section IV contains the conclusions. Finally detailed expressions of the mode coupling matrices are reported in the Appendix.

II. MODEL

A. Coupled-mode equations for VCSEL's

The stationary electromagnetic field is expanded on the complete and continuous basis of the TE and TM modes of an infinite medium with the characteristics of the passive cavity material:

$$\mathbf{E}(\rho,\phi,z)=\sum_{\alpha,l,p,m}\int dk\, A^{\alpha}_{kmpl}(z)\mathbf{E}^{\alpha}_{kmpl}(\rho,\phi), \qquad (1)$$

where k is the radial component of the wave vector and labels the continuous radial variation of the modes; index m labels the discrete azimuthal mode variation, while l indicates even and odd modes that differ in the $\cos(m\phi)$ or $\sin(m\phi)$ angular dependence; p labels TE and TM field distributions, and $\alpha=f,b$ forward and backward propagating waves. The explicit expressions of the cylindrical components of the vectorial modes $\mathbf{E}^{\alpha}_{kmpl}$ can be found in [25] and are reported in the Appendix.

The integral over k can be numerically discretized and the parameter $\mu=(k_n,m,p,l,\alpha)$ is introduced to label the mode amplitudes and mode distributions. In this way, expansion (1) can be rewritten in the compact form:

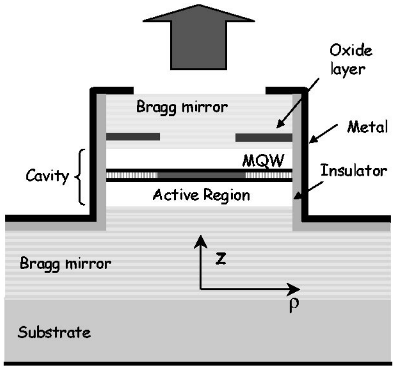

FIG. 1. Scheme of a VCSEL device.

$$\mathbf{E}(\rho,\phi,z)=\sum_{\mu} A_{\mu}(z)\mathbf{E}_{\mu}(\rho,\phi)\Delta k. \qquad (2)$$

The vector $\mathbf{A}=\{A_{\mu}\Delta k\}$ of the mode amplitudes is the unknown of the electromagnetic problem and is to be determined as the solution of the coupled-mode equations with proper boundary conditions.

As can be seen from the scheme reported in Fig. 1, the VCSEL device is particularly suitable to be analyzed by means of a coupled-mode approach. It in fact corresponds to a planar multilayer structure that defines the cavity and Bragg mirrors, with possible modifications of the transverse geometry. These include the gain profile in the active region, the oxide aperture, the etched top mesa mirror, and the metal contact rings; all of them contribute to define the lateral optical confinement. The shape and finite dimensions of the transverse geometry in each layer of the stack are introduced as transverse perturbations of well-defined profile in the laterally homogeneous reference medium.

According to coupled-mode theory [26], in each layer i of thickness L_i of the cascade structure, the vector of the mode coefficients is the solution of the equation

$$\frac{d\mathbf{A}}{dz}=(B+K_i\Delta k)\mathbf{A}, \qquad (3)$$

where Δk is related to the discretization of the transverse wave vector. B describes the free propagation in the reference material and is a diagonal matrix of elements $(B)_{\mu\mu'}=-is_{\alpha}\beta_{\mu}\delta_{\mu\mu'}$ where $s_{\alpha}=\pm 1$ for forward and backward waves and $\beta=\sqrt{k_r^2-k^2}$ is the longitudinal wave-vector component with $k_r=n_r\omega/c$, n_r the refractive index of the reference material, ω the angular frequency, and c the velocity of light. The coupling between the modes is introduced by the nondiagonal matrix K of elements [27]

$$(K)_{\mu\mu'}=-\frac{i\omega}{C_{\mu}}\int_S dS\Bigg\{\mathbf{E}_{\mu t}\cdot\Bigg[(\underline{\Delta\epsilon}\cdot\mathbf{E}_{\mu'})_t-\frac{(\underline{\Delta\epsilon}_{tz}\cdot\hat{z})(\underline{\Delta\epsilon}\cdot\mathbf{E}_{\mu'})_z}{\epsilon_c+\Delta\epsilon_{zz}}\Bigg]+\frac{E_{\mu z}\epsilon_c}{\epsilon_c+\Delta\epsilon_{zz}}(\underline{\Delta\epsilon}\cdot\mathbf{E}_{\mu'})_z\Bigg\}, \qquad (4)$$

where the indices t and z indicate transverse and longitudinal components of the vectors and C_μ is the power normalization constant and is given in the Appendix. The tensor $\underline{\Delta\epsilon}$ describes the perturbation to the homogeneous and isotropic reference dielectric permittivity, ϵ_r. The tensorial form accounts for the possibility of a nonisotropic perturbation related to some material anisotropy, induced, for example, by the electro-optic effect or by strain and thermal gradients in the structure. The information on the device injection and guiding geometries and dimensions is included in the model by defining, for each transversely nonhomogeneous layer of the structure, the profile of the perturbation $\underline{\Delta\epsilon}_{ij}(\rho,\phi,z)$.

With the assumption of an isotropic medium the expression of the perturbation $\underline{\Delta\epsilon}$ reduces to the simple form $\underline{\Delta\epsilon} = \Delta\epsilon\ \underline{I}$. In this case, the mode-coupling matrix can be split as the sum of a transverse and a longitudinal contribution, $K = K_t + K_z$, of elements

$$(K_t)_{\mu\mu'} = -\frac{i\omega}{C_\mu}\int_S \Delta\epsilon\mathbf{E}_{t\mu}\cdot\mathbf{E}_{t\mu'}dS,$$

$$(K_z)_{\mu\mu'} = -\frac{i\omega}{C_\mu}\int_S \frac{\epsilon_r\Delta\epsilon}{\epsilon_r+\Delta\epsilon_i}E_{z\mu}E_{z\mu'}dS, \tag{5}$$

where the term K_z applies only for TM modes and explicit expressions of the K_t matrix elements are derived in the Appendix. In the case of quasiplanar oxide confined structures, as the one presented in [28], the only two nonvanishing coupling matrix contributions are related, respectively, to the oxide diaphragm, and to the active region K_a.

When the perturbation $\Delta\epsilon$ is assumed to be a step function in the transverse plane, and therefore constant on a well-defined surface S for each layer, calculations are greatly simplified, since the angular integrals in Eq. (5) can be analytically performed. If this assumption is quite reasonable to describe the dielectric constant perturbation induced by the oxide window it is clearly very limiting for the description of the gain profile. More realistic injection profiles, which account for the carrier diffusion, can, however, be easily included in the model by approximating them with a staircase function.

B. Boundary conditions

The boundary conditions of the problem are fixed by the consistency of the forward and backward mode amplitudes at two reference interfaces. In particular, it is convenient to set these two sections to be the extreme lower $(z=0)$ and upper $(z=L)$ layer, beyond which the structure does not present any transverse perturbation and the geometry is planar. In this way, the layers above (below) $L(0)$ can be viewed as laterally homogeneous multilayer stacks and chain transmission matrix formalism can be applied to determine their reflectivity coefficient as a function of the wave vector k. The boundary conditions explicitly read

$$\mathbf{A}^f(0) = \Gamma_l\mathbf{A}^b(0),$$

$$\mathbf{A}^b(L) = \Gamma_u\mathbf{A}^f(L), \tag{6}$$

where the diagonal matrices Γ_l and Γ_u are the reflectivity coefficient components at, respectively, the lower and upper interfaces.

To find a closed form for the problem it is necessary to express the boundary conditions in terms of a single unknown; to this aim we introduce the formal relation between the mode amplitudes at the two reference interfaces as a cascade of single-layer solutions of Eq. (3),

$$\mathbf{A}(L) = T\mathbf{A}(0), \tag{7}$$

where the transmission matrix T is defined as

$$T = \prod_i e^{(B+K_i\Delta k)L_i} = \prod_i T_i \tag{8}$$

and the product is carried out on all the layers between the two considered sections.

It is convenient at this point to explicitly consider the dependence on the parameter $\alpha = f,b$. In this way, matrices B and K can be expressed in the form

$$B = \begin{pmatrix} B^f & 0 \\ 0 & B^b \end{pmatrix} \quad \text{and} \quad K = \begin{pmatrix} K^{ff} & K^{fb} \\ K^{bf} & K^{bb} \end{pmatrix}, \tag{9}$$

where the value of s_α in Eqs. (A1) and (A5) leads to the simple relations

$$K_t^{ff} = K_t^{fb} = -K_t^{bf} = -K_t^{bb},$$

$$K_z^{ff} = -K_z^{fb} = K_z^{bf} = -K_z^{bb}. \tag{10}$$

The same partition holds for the matrix T

$$T = \begin{pmatrix} T^{ff} & T^{fb} \\ T^{bf} & T^{bb} \end{pmatrix} \tag{11}$$

and when the formal solution (7) of the coupled-mode equation is combined with the boundary conditions (6), the complete electromagnetic problem is formulated by the equation

$$(T^{bf}\Gamma_l + T^{bb})\mathbf{A}^b(0) = \Gamma_u(T^{ff}\Gamma_l + T^{fb})\mathbf{A}^b(0). \tag{12}$$

Moreover, the very small thickness of the multiple-quantum-well (MQW) active region $(d \ll \lambda)$ allows a linear expansion of the active-layer contribution to T,

$$T_a \simeq e^{(B+K_{al}\Delta K)d} + K_{ag}d\Delta k, \tag{13}$$

where the coupling coefficient in the active layer K_a has been split as the sum of a constant term K_{al}, corresponding to the losses at zero carriers, and a term K_{ag} that accounts for the carrier-induced dielectric constant perturbation in the active region. The peak value $(\Delta\epsilon_a)$ of the perturbation is the unknown of the electromagnetic problem and has to be determined for each cavity mode as a solution of the mode threshold conditions while its transverse variation is related to the carrier density profile and therefore vanishes where the carriers go to zero.

By extracting the unknown quantity $\Delta\epsilon_a$ we define

$$K_{ag}\Delta K = -ik_r\frac{\Delta\epsilon_a}{\epsilon_r}K'_{ag}. \tag{14}$$

Correspondingly, also matrix T can be split as the sum of a passive well-known contribution labeled with 0, and an active contribution labeled with λ, which contains the problem unknown:

$$T = T_0 + \lambda^{-1}T_\lambda. \tag{15}$$

T_0 is simply defined as the matrix T in the absence of carriers, while T_λ is of the form

$$T_\lambda = \prod_b T_j K'_{ag} \prod_t T_j, \tag{16}$$

where the subscripts b and t indicate that the products are extended to the layers below and above the active region. The unknown $\Delta\epsilon_a$ is related to λ by

$$\lambda = -ik_r d\frac{\Delta\epsilon_a}{\epsilon_r}. \tag{17}$$

With this definition the boundary condition (12) finally results in an eigenvalue problem for $\mathbf{A}^b(0)$ of the form

$$\lambda\mathbf{A}^b(0) = M_0^{-1}M_\lambda\mathbf{A}^b(0), \tag{18}$$

where

$$M_j = T_j^{bb} - \Gamma_u T_j^{ff}\Gamma_l + T_j^{bf}\Gamma_l - \Gamma_u T_j^{fb} \quad (j = 0,\lambda). \tag{19}$$

The real and imaginary parts of the complex eigenvalues provide, respectively, the refractive index variation and material gain for each eigenmode of the problem. Very often in the literature, the change of refractive index induced by the carriers in the active region is neglected, and the effectively lasing modes are selected as the eigenmodes with $\mathrm{Im}(\lambda) = 0$: the discrete frequencies at which these solutions are found fix the lasing mode frequencies and the corresponding imaginary parts of the eigenvalues give the mode threshold gains. In the following section the validity of this approximation will be discussed and results will be compared with those provided by a self-consistent method in which the active material optical response is taken into account. The eigenvectors $\mathbf{A}^b(0)$ are complex due to the presence of the gain region and, by means of expansion (1), they allow the reconstruction of the field distributions at $z = 0$ for the different modes and, through Eq. (3), in any other section.

C. Self-consistent solution

The QW optical response as a function of the frequency ω and carrier density N is determined by applying the microscopic model developed in [29] to the particular QW structure of the device. The obtained expression for the complex dielectric constant is of the form

$$\Delta\epsilon_a = \frac{1}{\pi d}\int dk_e\, k_e\frac{M_{k_e}^2}{\hbar}\frac{[f_{ck_e}(N) - f_{vk_e}(N)]}{(\omega_{k_e} - \omega) - i\gamma_p}, \tag{20}$$

where k_e indicates the carrier transverse momentum component. The transition dipole matrix elements (M_k), the transition energies $(\hbar\omega_k)$, and the Fermi-Dirac quasiequilibrium distributions in conduction and valence bands (f_{ck}, f_{vk}), have been computed from the QW band structure and depend on the QW composition and size. Moreover, the spectral dependence of the polarization relaxation rate γ_p is taken into account [30], and Coulomb effects are introduced only as regards band-gap renormalization.

The requirement that the solutions of the electromagnetic problem match the QW optical response introduces a self-consistent mechanism of the selection of the lasing modes. The frequency at which this requirement is fullfilled, for a certain value of carrier density, fixes the modes proper frequency (ω_0) and threshold carrier density (N_{th}) for each cavity mode

$$\lambda^{-1}(\omega_0) = -ik_r d\frac{\Delta\epsilon_a(\omega_0, N_{th})}{\epsilon_r}. \tag{21}$$

The self-consistent solutions are now compared to those obtained by the simple requirement $\mathrm{Im}(\lambda) = 0$ and the range of validity of this commonly adopted approximation is analyzed. We expect the discrepancy between the two methods to depend on the detuning condition between the cavity resonance and the active material optical response, determined by the device construction properties and by the operating temperature. In Fig. 2 we therefore report the threshold power gains vs lasing wavelengths of the first five radial modes with no azimuthal variation (in LP notation 0-1, 0-2, 0-3, 0-4, 0-5) for seven material configurations $(a-g)$. These are characterized by different values of the gap $\lambda_g = \lambda_{g0} + \Delta\lambda$, where $\Delta\lambda$ varies around $\Delta\lambda = 0$ which corresponds to the reference optical response, computed for a 5-nm $\mathrm{In}_{0.12}\mathrm{Ga}_{0.88}\mathrm{As}$ strained QW with band-gap wavelength $\lambda_{g0} = 0.97\,\mu\mathrm{m}$ and relaxation rate $\gamma_p = 1.35\times10^{13}\,\mathrm{s}^{-1}$. These results refer to the 3D VCSEL structure described in Sec. III A with a pillar radius of 4 μm and an oxide aperture radius of 2 μm. The active section is characterized by a step carrier profile with the size of the oxide window; this results in gain (losses) inside (outside) the active region. The self-consistent solutions are directly compared with the results obtained with the approximate method. With respect to the mode threshold power gains, the two methods provide only slight differences and a common qualitative behavior is observed. The mode threshold gains increase with $\Delta\lambda$ due to the increasing losses in the QW. The self-consistent solution, however, provides the additional information of the modes that can actually reach the lasing condition: To this end in Fig. 2 (middle) the maximum gain provided by the QW is also reported so that only the modes with threshold gain below this value can lase. Moreover, the two methods result in significant differences as regards the mode wavelengths since the self-consistent solution shows a dispersive behavior for varying $\Delta\lambda$ not included in the approximate approach. This is related to the change of the refractive index Δn induced by the carrier density and the observed s-shaped behaviors in the λ-G plane [see Fig. 2 (up)] indicate the passing of the mode wavelength through an extremum of Δn. Fi-

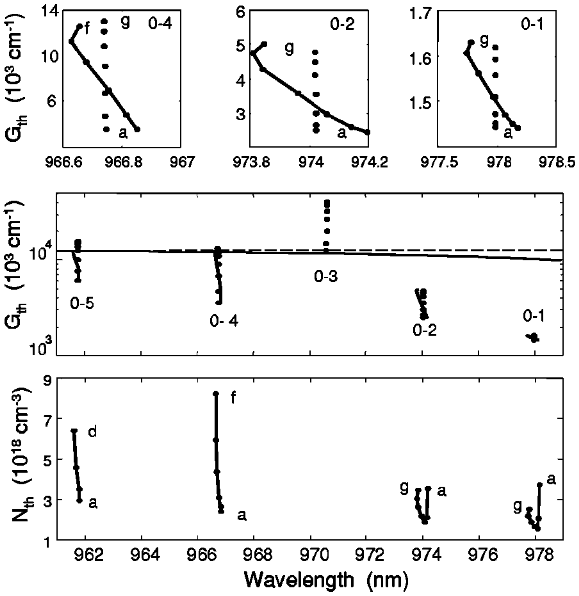

FIG. 2. Wavelengths, material threshold gains (upper part), and corresponding carrier densities (lower part) of modes in the 3D VCSEL: continuous lines are the self-consistent solutions, dots are the approximate results. Different optical responses with $\Delta\lambda$ (see text) from -30 nm (*a*) to $+30$ nm (*g*) with 10-nm steps are considered. The small upper graphs are expansions of the graph in the middle, which shows also the maximum gain provided by the QW in the two limiting detunings *a* (continuous line) and *g* (dashed line).

nally, as a result of the self-consistent solution we show in Fig. 2 (down) the corresponding threshold carrier densities. The minimum for each mode is found at the detuning for which the mode wavelength matches the material gain peak.

D. Approximated scalar model

Scalar models are very commonly adopted for their lower complexity; they well describe the laser modes and threshold properties in the limit of large aperture devices, with radius $a \gg \lambda$, and of small transverse index variations. In these limits, in fact, the wave vector k is very small and so TE and TM modes can be treated as TEM. In this section we will show how the vectorial model presented in this paper reduces to a simplified one, when the TEM approximation is introduced. This will lead to a mode expansion directly performed on an approximate basis of linearly polarized (LP, [25]) modes.

As a first step it is useful to express the mode expansion (1) in the following equivalent form:

$$\mathbf{E}=\sum_{klm\alpha}\tfrac{1}{2}[A^{\mathrm{TE}}_{\mu_-}\mathbf{E}^{\mathrm{TE}}_{\mu_-}+sA^{\mathrm{TM}}_{\mu_-}\mathbf{E}^{\mathrm{TM}}_{\mu_-}+A^{\mathrm{TE}}_{\mu_+}\mathbf{E}^{\mathrm{TE}}_{\mu_+}+sA^{\mathrm{TM}}_{\mu_+}\mathbf{E}^{\mathrm{TM}}_{\mu_+}], \tag{22}$$

where the expansion over the index p has been explicated, $\mu_{\pm}=\{k,l,m\pm 1,\alpha\}$ and $s=\pm 1$. In the TEM approximation the longitudinal field component E_z is set to zero and the K_z contribution to the coupling coefficient matrix, typical of TM modes, vanishes. Moreover, (see Appendix), the modal impedances are set equal, $Z^{\mathrm{TE}}=Z^{\mathrm{TM}}$, and give rise to common normalization constants, $C^{\mathrm{TE}}_{\mu}=C^{\mathrm{TM}}_{\mu}$, and to common reflectivity coefficients $\Gamma^{\mathrm{TE}}_{\mu}=\Gamma^{\mathrm{TM}}_{\mu}$. In this way, the coupled-mode equation (3) and the associated boundary conditions (6) do not distinguish between TE and TM polarizations, and the solutions of the eigenvalue problem (18) $(\mathbf{A}^{\mathrm{TE}},\mathbf{A}^{\mathrm{TM}})$ are found to satisfy the following conditions:

$$\begin{aligned} A^{\mathrm{TE}}_{\mu_-}&=sA^{\mathrm{TM}}_{\mu_-}=A^{\mathrm{TEM}}_{\mu_-},\\ A^{\mathrm{TE}}_{\mu_+}&=-sA^{\mathrm{TM}}_{\mu_+}=A^{\mathrm{TEM}}_{\mu_+}. \end{aligned} \tag{23}$$

If the explicit expressions (A1) of the modes are introduced, and relations (23) are taken into account, expansion (22) becomes of the form

$$\mathbf{E}=\sum_{k,lm,\alpha} J_{mk}[(A^{\mathrm{TEM}}_{\mu_-}+sA^{\mathrm{TEM}}_{\mu_+})f_{lm}\hat{\mathbf{x}}+(A^{\mathrm{TEM}}_{\mu_-}-sA^{\mathrm{TEM}}_{\mu_+})g_{lm}\hat{\mathbf{y}}]. \tag{24}$$

From the structure of the coupling matrix given in the Appendix [see Eq. (A15) therein], it also follows that

$$A^{\mathrm{TEM}}_{\mu_-}=A^{\mathrm{TEM}}_{\mu_+}. \tag{25}$$

The value of the parameter s therefore selects one particular polarization direction in Eq. (24) and the approximate vectorial model becomes equivalent to a scalar model in which the mode expansion is directly performed on the basis of the linearly polarized $\mathcal{P}$ modes

$$E(\rho,\phi,z)=\sum_{lm}\int dk\,B_{klm}(z)\mathcal{P}_{klm}(\rho,\phi), \tag{26}$$

where

$$\mathcal{P}_{klm}=J_m(kr)\times\begin{cases} f_{lm}(\phi)\hat{\mathbf{x}}\\ g_{lm}(\phi)\hat{\mathbf{y}}.\end{cases} \tag{27}$$

In order to discuss the range of validity of the LP approximation, the mode threshold properties obtained by the scalar approach are compared to those of the fully vectorial model. In particular, in Fig. 3 we report the threshold gains and lasing wavelengths of the first five radial modes at the azimuthal order $m=0$ for LP and vectorial solutions. As expected, the differences on the threshold properties increase with increasing radial order: for modes 0-1 and 0-2 they are practically negligible, since the dominant spectral components of these modes are peaked around $k=0$ where the TEM approximation holds. Starting from the third radial order instead, the approximated scalar approach gives rise to relevant errors in evaluating the mode threshold gain and wavelength and the fully vectorial model is required.

E. Far fields

The free propagation of the electromagnetic field outside the cavity is given by

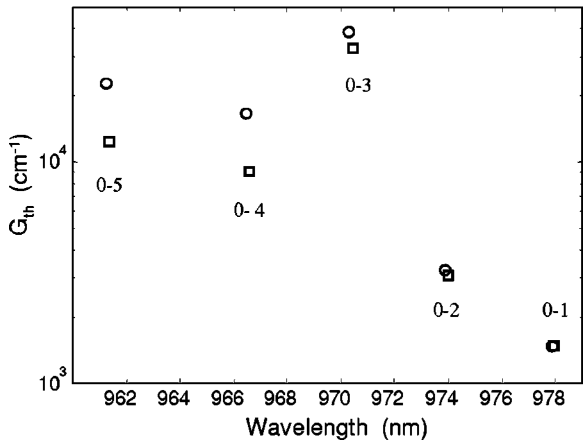

FIG. 3. Material power gains and wavelength for radial modes with no azimuthal variation; comparison between vectorial (circles) and scalar (squares) models. The 3D structure described in Sec. III A is analyzed with a 8-μm mesa upper mirror and 4-μm oxide aperture diameter at a field antinode.

$$\mathbf{E}(\rho,\phi,z)=\sum_{l,p,m}\int dkA^{f}_{kmpl}(L)\mathbf{E}_{kmpl}(\rho,\phi)e^{-i\beta_0 z}, \tag{28}$$

where β_0 is the propagation constant in air. Each point (ρ,ϕ,z) in $\mathbf{r}$ space is equivalently defined in the spherical system of coordinates by

$$\theta_r=\tan^{-1}\left(\frac{\rho}{z}\right),\quad R=\sqrt{\rho^2+z^2},\quad \phi. \tag{29}$$

and correspondingly each point (k,β) in $\mathbf{k}$ space is defined by

$$\theta_k=\tan^{-1}\left(\frac{k}{\beta_0}\right),\quad k_0=\sqrt{k^2+\beta_0^2}. \tag{30}$$

Since the far fields are analyzed at a distance $z\gg\lambda$ from the emission plane, all the contributions to the electric field deriving from $\theta_k\neq\theta_r$ cancel out at each point (ρ,ϕ,z). It is therefore sufficient in Eq. (28) to perform the integration only around the value $\bar{k}=k\sin(\theta_r)$, and assume A_{klpm} constant to its value in $\bar{k}$. In this way, expression (28) for the field becomes

$$\mathbf{E}(\rho,\phi,z)=\int dk\, e^{-i\beta_0 z-ik\rho}\sum_{l,p,m}A^{f}_{\bar{k}mpl}(L)\mathbf{E}_{\bar{k}mpl}(\rho,\phi)e^{i\bar{k}\rho}. \tag{31}$$

In the above assumption $\theta_k\simeq\theta_r$, where $i\beta_0 z+ik\rho=ik_0R\cos(\theta_k-\theta_r)\simeq ik_0R[1-\frac{1}{2}(\theta_k-\theta_r)^2]$, the integration in the radial component can be analytically performed,

$$F(\rho,z)=\int dk\, e^{-i\beta_0 z-ik\rho}\simeq\sqrt{\frac{i2\pi k_0}{R}}\cos\theta_r e^{-ik_0R}. \tag{32}$$

Asymptotically, for $(\rho,z\rightarrow\infty)$, for instance E_x is given by

$$\begin{aligned}E_x(\rho,\phi,z)=F(\rho,z)\sum_{l,m}e^{i\bar{k}\rho}\{&f_{m+1,l}(\phi)J_{m+1}(\bar{k}\rho)\\&\times(A^{p=\mathrm{TE}}_{\bar{k}lm}-A^{p=\mathrm{TM}}_{\bar{k}lm})-f_{m-1,l}(\phi)J_{m-1}(\bar{k}\rho)\\&\times(A^{p=\mathrm{TE}}_{\bar{k}lm}+A^{p=\mathrm{TM}}_{\bar{k}lm})\}.\end{aligned} \tag{33}$$

For $\rho=0$, however, the above approximation cannot be used since the contribution from $\bar{k}=0$ is zero. The far-field expression in this case must be numerically evaluated.

III. NUMERICAL RESULTS

A. VCSEL structure

The scheme of the device preliminarily analyzed is the very general one proposed in [28]. Different modeling approaches (see, for instance, [24]) have already been applied to describe its threshold features and, for this reason, it is particularly suitable to test the validity of our model. In particular, a paper comparing the results from different models is in preparation in the framework of the European project COST 268.

It is essentially a planar structure in which two infinitely extended Bragg mirrors ($\mathrm{Al}_x\mathrm{Ga}_{1-x}\mathrm{As}$/GaAs pairs of λ/4 layers) define a GaAs λ cavity, at $\lambda=980$ nm. The active region at the cavity center contains a 5-nm QW and the transverse carrier confinement is achieved by means of a thin λ/20 oxidized AlAs window of circular geometry, incorporated into the first $\mathrm{Al}_x\mathrm{Ga}_{1-x}\mathrm{As}$ layer of the top mirror. The values of the oxide aperture radius a and position of the oxide window x within the layer, from a node to an antinode position, are left to be variable parameters in the numerical simulations. The data on the position, thickness, transverse dimensions, material composition, and optical properties of the different structure layers are defined in Table I. Due to the circular geometry of this structure, the computation of the coupling coefficients matrices (5) can be carried out analytically in terms of Bessel functions and the modes with different azimuthal variation m do not couple, so that one can solve the eigenvalue problem for different fixed m values. The numerical simulations will then be extended to describe more complex and realistic 3D VCSEL structures as the one depicted in Fig. 1. In particular, we consider a device derived from the one described in Table I but with a mesa upper mirror and cavity. The structure is then cladded by a 300-nm insulator layer and covered with a 100-nm metallization. The effect of different structure elements, such as the metallization, the dimensions of the top mesa mirror and the asymmetric shape of the oxide aperture (for example, elliptical or rectangular) will be separately analyzed. The only drawback in dealing with noncircular geometries is that the azimuthal modes are now coupled together and the coupling coefficients matrices (5) have to be computed numerically. The numerical complexity of the problem is determined by the number of azimuthal harmonics that are to be included, and therefore strongly depends on the degree of asymmetry of the structure under analysis.

TABLE I. Quasiplanar VCSEL structure as proposed in [28].

	Thickness (nm)	Material	Index	
Air		Air	1	
24 pair DBR	69.49	GaAs	3.53	
	79.63	Al_x-Ga_{1-x}-As	3.08	
Oxide window	69.49	GaAs	3.53	
	$63.71 - z_{ox}$	Al_x-Ga_{1-x}-As	3.08	
	15.93	AlAs	2.95	$r < a$
		AlOx	1.60	$r > a$
	z_{ox}	Al_x-Ga_{1-x}-As	3.08	
Lambda cavity	136.49	GaAs	3.53	
	5.00	QW	$3.53 + i n_{gain}$	$r < a$
			$3.53 - i0.01$	$r > a$
	136.49	GaAs	3.53	
29.5 pair DBR	79.63	Al_x-Ga_{1-x}-As	3.08	
	69.49	GaAs	3.53	
Substrate		GaAs	3.53	

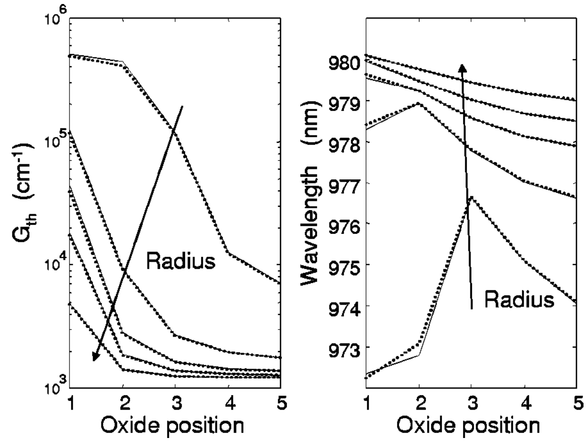

FIG. 4. Fundamental mode material power gains (left) and wavelengths (right) vs oxide position (1: node; 5: antinode) for different oxide aperture radii ($a = 0.5$, 1, 1.5, 2, and 3 μm). The VCSEL structure is described in Table I. Continuous (dotted) lines refer to the vectorial (scalar) model.

B. Quasiplanar structures

In this section we investigate the effects of the oxide diaphragm on the mode optical confinement by performing a parametric study of the laser threshold properties upon changing the longitudinal position and the radius of the aperture. Referring to the quasiplanar structure defined in Table I, in Fig. 4 we report the threshold gain (left) and lasing wavelength (right) of the fundamental mode for five values of the aperture radius and five values of the oxide position within the $Al_xGa_{1-x}As$ layer. As expected, the mode threshold gain and the detuning of the lasing wavelength with respect to the designed cavity value, $\lambda = 980$ nm, are decreasing functions of the aperture radius, for each fixed position of the oxide diaphragm. The threshold gain asymptotically tends, for large radii, to its planar limit; in the particular case where the oxide layer is at the antinode of the electromagnetic field (position 5) this condition is recovered already for very small radii ($a = 1.5$ μm) due to the strong index guiding effect. Similarly, for each fixed size of the oxide aperture, the mode confinement increases as the oxide is moved away from the field node position, and the threshold gain is a monotonically decreasing function with a minimum in the field antinode configuration. As regards the wavelength detuning instead, the progressive change of the oxide position from a node to an antinode of the field gives rise to two competing effects that can well explain the nonmonotonic behavior observed in Fig. 4 (right): the increasing transverse-mode confinement and the increasing longitudinal overlap between the optical field and the oxide layer. The first results in a decreasing wavelength detuning due to the reduced transverse overlap of the field with the oxide layer and is a relevant effect only in the case of reduced aperture radii where the mode is weakly confined. The second instead is present in all devices and gives rise to a monotonically increasing wavelength detuning.

The results obtained by applying the full vectorial model (which provides two degenerate solutions indicated by the continuous line) are directly compared with those obtained in the scalar linearly polarized approximation (dotted line). The observed differences between the two approaches are almost negligible, and only slightly increase in the cases of the smallest aperture dimensions. This result confirms that for the fundamental mode, as already shown in Fig. 3, the scalar approach can be applied on a wide range of structure parameters.

In the same way, in Fig. 5 the threshold properties of the first-order transverse mode are studied. The behavior of the gains and wavelengths for the smallest device are almost constant and with very high values, since the confinement is very poor wherever the oxide is positioned. It must here be underlined that in these results the QW optical response is not accounted for. So gains on the order of $10^5 - 10^6$ cm^{-1} are not realistic since the maximum gain provided by a QW is on the order of 10^4 cm^{-1}. Instead, for the other aperture values, the behavior is similar to the fundamental mode case, but higher values of the threshold gain and wavelength detuning are found. Only for radii greater than 1.5 μm and oxide position 3, 4, and 5 the gain difference becomes smaller and mode competition can arise. The vectorial treatment results in two nondegenerate solutions that cannot be resolved by the scalar approach: the two orthogonally polarized fields correspond to a purely TE and purely TM mode and the degeneracy is therefore lifted by the different modal impedances, mirror reflectivities, and coupling coefficients. The results presented in Figs. 4 and 5 are in very good agreement with those reported in [24] for the 4-μm-diam aperture structure.

The effect of the metal contact ring on the laser performances is now discussed by comparing the threshold properties and the emitted field distributions. In particular, in Fig. 6 we report the field profiles of modes 0-1 and 0-2 inside the

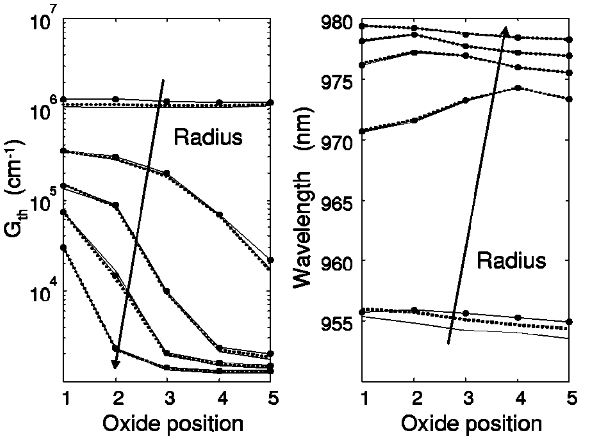

FIG. 5. Same as in Fig. 4, but for first-order mode; in this particular case there are two vectorial solutions: TE (continuous lines) and TM (continuous lines with dots).

cavity and externally emitted, in the presence and absence of the metal contact. These results are obtained by adopting the approximated scalar approach since, as shown in Fig. 3, this is a good approximation for these first two modes. The effect of the metal ring, practically negligible on the internal fields, provides instead a cut and a distortion on the profile of the emitted field. Moreover, the corresponding threshold gains and lasing wavelengths of the two modes in the two cases are reported for comparison. The presence of the additional metal layer introduces an absorption effect in the top mirror, clearly stronger for the less confined mode; the effect on the lasing wavelength is very small.

C. 3D structures

We now consider the more realistic 3D device described in Sec. III A with an etched top mesa mirror of circular geometry and metal ring contact. The oxide aperture and metal ring inner radius are kept fixed to 2 μm, while the radius of the pillar is varied in the numerical simulations. The effect of the pillar dimensions on the laser performance is well understood if the threshold properties are analyzed in connection to the corresponding field profiles. In this case the numerical effort due to the complexity of the structure is reduced by introducing the LP approximation; anyway the differencies between the LP and vectorial model have already been outlined when discussing Fig. 3. In Fig. 7 the threshold gains and wavelengths of the first four cavity modes are reported for three values of the pillar radius. Correspondingly, in Figs. 8(A)–8(C) we report the cuts of the circularly symmetric field profiles of these modes in correspondence of the QW. The fundamental mode $\mathcal{P}_{0-1}$ is completely confined within the oxide aperture and its threshold gain has a weak dependence on the pillar dimensions: the solutions are nearly coincident with the quasiplanar cavity solution. The modes of higher radial orders instead start to spread out beyond the injected region, as can be seen in Fig. 8, and the strongly

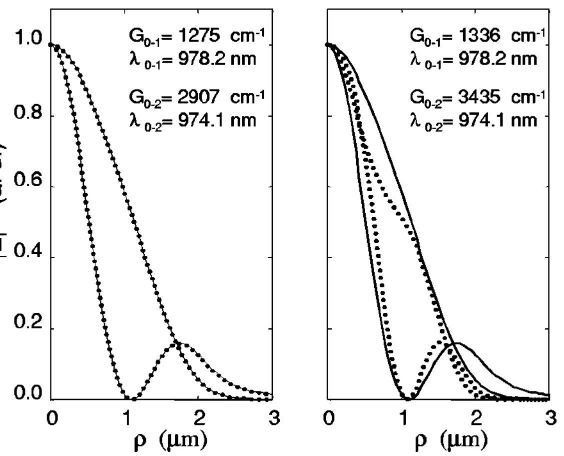

FIG. 6. Normalized field intensity of the first two radial modes with zero azimuthal order at the cavity center (continuous lines) and at the output (dotted lines). We consider the 4-μm oxide diameter aperture quasiplanar structure of Table I (left) and a similar device (right), but with a 100-nm metalization on top with an output window the same as that in the oxide.

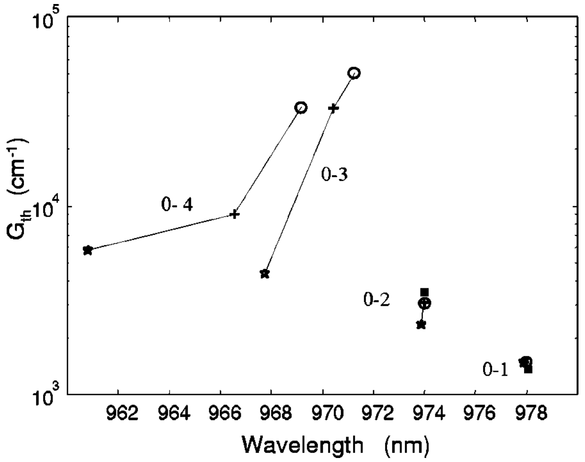

FIG. 7. Power gains and wavelengths of $\mathcal{P}_{0-n}$ modes in the 3D VCSEL (see Sec. III A) for different pillar radii: 3 (stars), 4 (crosses), and 5 μm (circles). The quasiplanar case with metalization (black squares) is also reported for comparison.

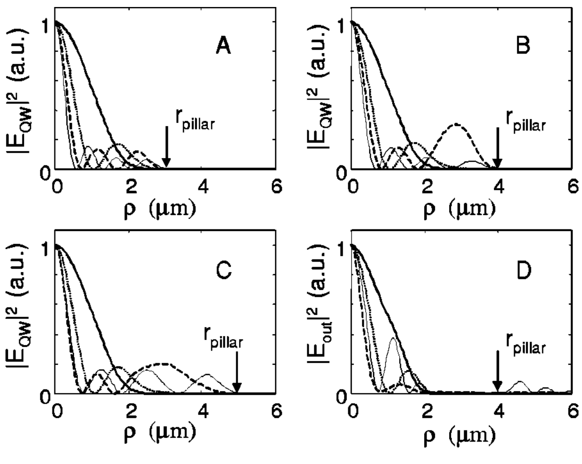

FIG. 8. Intensity field profiles at the cavity center of the modes of Fig. 7; A, B, C correspond to the three pillar radii, respectively. The graph D is the output corresponding to B.

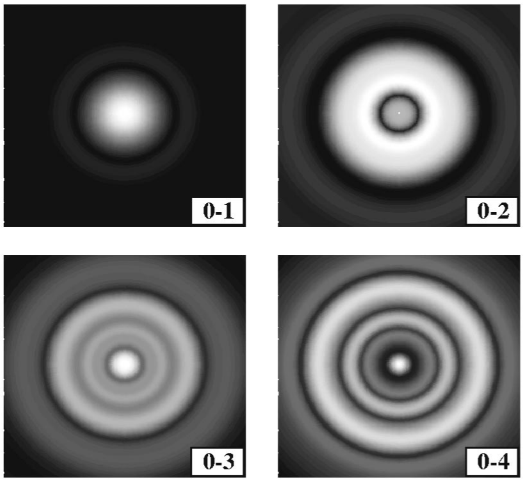

FIG. 9. Far-field distributions at 10 cm from the output section corresponding to the near fields of Fig. 8(D); the image side is 20 cm.

reduced transverse confinement explains the significant increase in the threshold gain observed in Fig. 7. The possible nonmonotonic gain increase with radial order (third mode) is related to a sort of ''pillar mode,'' as can be clearly seen in Figs. 8(B) and 8(C) (dashed lines), where a strong field is located in the pillar ring outside the active region. The same phenomenon was already found in the results presented in Fig. 3. When the confinement effect provided by the pillar becomes dominant the threshold properties are strongly dependent on its dimensions: the mode threshold gain increases and the wavelength detuning decreases for increasing pillar radius. In Fig. 8(D) we also report the near-field profiles of the four modes, externally emitted from the VCSEL. The results refer to the structure with pillar radius 4 μm. The cut and the field distortion provided by the metal ring can be observed and, in the case of weakly confined higher-order modes, the field distribution emerges beyond the metal ring. Examples of far-field profiles are reported in Fig. 9 for the same near-field distributions of Fig. 8(D).

D. Noncircular structures

In the last set of results, the mode threshold properties and field distributions are investigated for VCSEL devices with noncircular oxide apertures and the influence of shape asymmetry on polarization and mode selection is discussed [13,31]. In particular, computations have been performed by using the fully vectorial model on rectangular and elliptical structures with variable size and axis ratio. Results will be reported for the fundamental and first-order mode because of their particular interest with respect to switching and bistability mechanisms in VCSEL's [9–12].

In Fig. 10 the near-field components of the fundamental mode are reported for an elliptical and rectangular structure; the *x* coordinate is aligned with the longer axis and the white lines represent the oxide aperture. In both cases, all vectorial solutions are characterized by the three components of the electric field which give rise to an inhomogeneous polarization state [15]; however, for the considered size, one component is strongly dominant over the others of at least four orders of magnitude and the two fields can practically be considered as linearly polarized along orthogonal directions. Differences in the field profiles of the two solutions, observed especially on the weaker components, indicate that the degeneracy between the two orthogonally polarized solutions, characteristic of circular geometries, is here lifted due to the asymmetry of the structure.

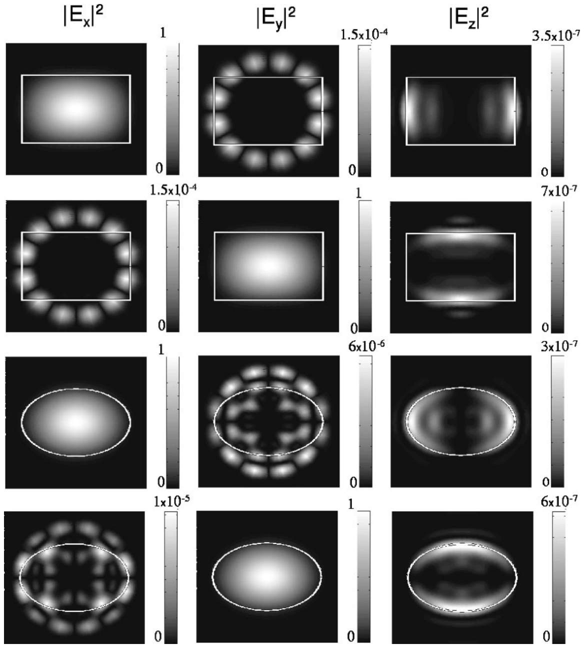

FIG. 10. Fundamental mode intensity distributions related to the quasiplanar structure with the oxide in position 5 (antinode); the active region and oxide aperture are taken either rectangular or elliptical with a smaller axis set to 4 μm and 1.5 axis ratio.

The threshold properties of these two orthogonally polarized modes are analyzed in detail in the following figures, with particular attention to the influence of oxide position, aperture size, and asymmetry (ellipse axis ratio) on the dichroism and birefringence. In Fig. 11 the threshold gain and lasing wavelength of the fundamental modes are studied for varying axis ratio in the elliptical and rectangular structures described above. Decreasing threshold gains and wavelength detunings from the nominal cavity wavelength (980 nm) are obtained at increasing axis ratio due to the corresponding increased aperture area. For the same reason at equal axis ratio the values of the rectangular structure are smaller with respect to the elliptical structure. Moreover, as expected, in the limit of circular devices (unity axis ratio), the orthogonally polarized solutions become degenerate in gain and frequency. In order, however, to better investigate the gain and wavelength differences between orthogonally polarized modes arising from the structure asymmetry, which are not evident in the adopted scale, the values of dichroism and birefringence are directly reported in the following plots. In particular, we will now refer to the results obtained for the elliptical structure.

In Fig. 12 (upper plots) the oxide position is set at the antinode position 5 and the percentage gain difference and birefringence between the two orthogonal polarizations of

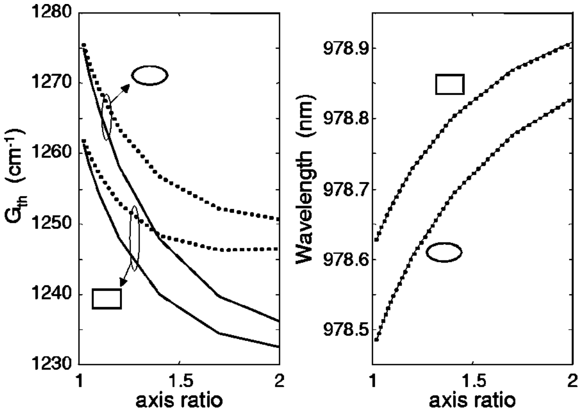

FIG. 11. Fundamental mode power gains (left) and wavelengths (right) vs axis ratio for the structures of Fig. 10. The continuous and dashed lines indicate, respectively, the *x* and *y* polarizations.

the fundamental mode are analyzed as a function of the ellipse minor axis for three different values of the axis ratio. Both dichroism and birefringence are decreasing functions of the aperture size and become very small for values of the minor axis above 6 μm. On the contrary, for reduced aperture dimensions the values of birefringence and dichroism rapidly increase and become of comparable order to those typically induced by other effects, such as material anisotropies related to strain [32] and electro-optic effect [33]. The contribution of shape asymmetry to polarization competition can therefore play a crucial role in the case of small aperture devices. In addition, the effect is enhanced for increasing axis ratio and a strong polarization control is expected to be achieved with high degrees of asymmetry in small aperture devices. The degree of asymmetry that can be introduced in realistic structures is, however, limited by the requirement of circularly symmetric beam profiles, desirable in many applications, and $b/a=2$ can be taken as a reasonable upper limit for the axis ratio.

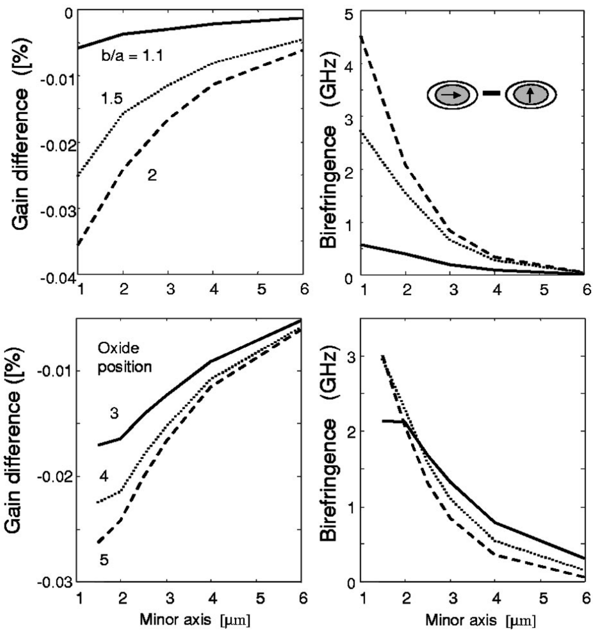

FIG. 12. Parametric study of birefringence and gain difference induced on the fundamental mode by an elliptical shape of the active region and oxide aperture. Effect of the axis ratio for the oxide window in position 5 (upper part) and of the oxide position for an axis ratio of 1.5 (upper part) vs minor axis.

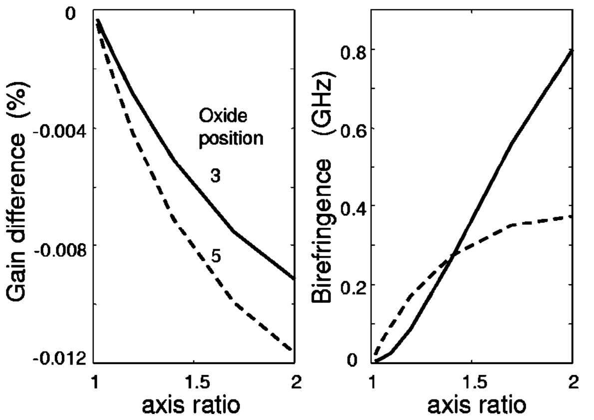

FIG. 13. Similar to Fig. 12, but vs the axis ratio for a 4-μm minor axis.

In Fig. 12 (lower plots) the axis ratio is kept fixed at 1.5 and we vary the oxide position. The dependence on minor axis is similar to the case of the upper plots. As regards the behavior vs the oxide position, the gain difference is larger the stronger the confinement whereas the birefringence presents more complicated features, which can also be seen in Fig. 13 where we vary the axis ratio, for two positions of the oxide. The highest birefringences are achieved for the more distorted spatial field distributions; these depend both on the aperture shape and the field transverse confinement. For small axis ratios the oxide position 3 provides a poor confinement, and so a lower birefringence. For higher axis ratios, the strong confinement of the oxide in position 5 prevents the field from following the aperture shape, while this is still possible for the lower confinement structure: this results in an inversion of the birefringence characteristics.

In Fig. 14 the near-field distributions of the first higher-order mode are reported for the elliptical structure. Four nondegenerate solutions are found, the dominant components of which describe two orthogonally oriented two-lobed distributions, each linearly polarized along two orthogonal directions. The threshold properties as well as the gain and wavelength differences between these different solutions are analyzed in Fig. 15 for varying axis ratio. In the upper plot of Fig. 15 wavelength and threshold gains of the four nondegenerate modes are reported: continuous and dotted lines describe, respectively, *x* and *y* polarization while the different spatial distributions are indicated with the schematic drawings in the plot. Modes with the orthogonal polarization and different field distributions are degenerate in the limit of circular structures, and then show increasing dicroism and birefringence for increasing axis ratio. The very high values observed indicate that the effect of shape asymmetry on the selection of the field spatial distribution is very strong. On the other hand, birefringence and dichroism between orthogonally polarized modes with the same spatial distributions are reported in the lower plots of Fig. 15 where the

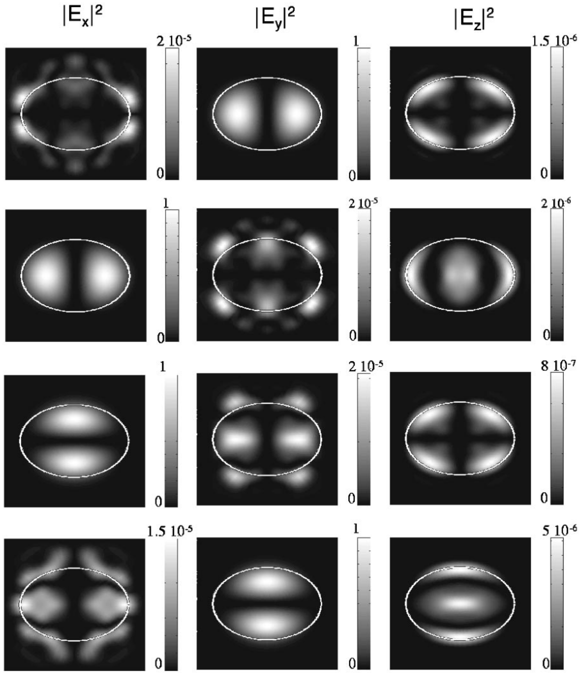

FIG. 14. First higher-order field distributions related to the quasiplanar structure with the oxide in position 5 (antinode); the active region and oxide aperture are elliptical with a 4 μm smaller axis and 1.4 axis ratio.

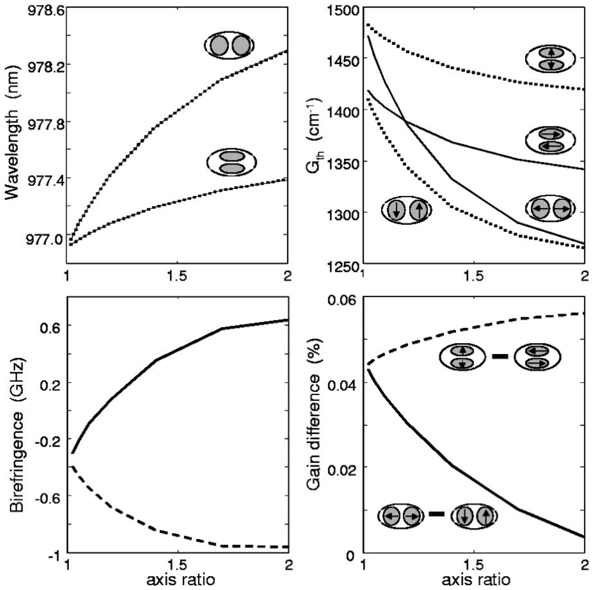

FIG. 15. First higher-order mode characteristics of the elliptical VCSEL vs axis ratio for a 4-μm minor axis and oxide position 5. Upper part, wavelengths and threshold gains; lower part, corresponding bireferingence and percentage gain difference.

continuous and dashed lines indicate, respectively, the horizontally and vertically oriented two-lobed field distributions. For these particular modes, solutions are purely TE and TM in the limit of unitary axis ratio and a percentage gain difference (0.04%) and a slight birefringence (0.4 GHz) are found. These increase with the axis ratio, with opposite sign for the two orthogonal spatial distributions. The mode that fills the ellipse in the direction of major axis is more sensible to variations of the ellipticity and a higher variation of birefringence and dichroism with the aperture asymmetry is observed.

IV. CONCLUSIONS

In this work we have proposed a comprehensive method to model VCSEL devices accounting for their complete 3D geometries and preserving the full vectorial character of the electromagnetic field. The model is based on the expansion of the field in the continuous basis of the cylindrical TE and TM modes of the cavity region, and on the application of coupled mode theory. The electromagnetic problem, determined by the self-consistency relation between forward and backward waves at the mirror discontinuities, is in this way reduced to an eigenvalue problem which can be easily handled. The complex eigenvalues determine the required mode gain, lasing frequency, and carrier threshold density, while the eigenvectors give the field distribution inside the resonator and, consequently, the radiated field.

The validity of a scalar approach was discussed by comparing it with the fully vectorial model and we found a good agreement only for low-order modes. The influence of the device construction characteristics on the laser threshold properties has been studied and interesting results have been obtained for the fundamental and first-order mode by changing the position and size of the oxide window, metallization, and mesa dimensions. Particular attention was given to noncircular devices and their effect on birefringence and dichroism was studied.

ACKNOWLEDGMENTS

The activity reported has been carried out in the framework of VISTA (HPRN network) and MADESS II (Progetto Finalizzato of Italian CNR).

APPENDIX: COUPLING COEFFICIENTS

In this appendix the matrix elements of the coupling coefficient matrix, K_t^{ff}, are computed. To this aim it is useful to report the expression of the expansion modes [25],

$$E_r=\left[(1+s_p)\frac{m}{k\rho}J_m(k\rho)+(1-s_p)J_m'(k\rho)\right]f_{ml}(\phi),$$

$$E_\phi=\left[(1-s_p)\frac{m}{k\rho}J_m(k\rho)+(1+s_p)J_m'(k\rho)\right]g_{ml}(\phi), \qquad \text{(A1)}$$

$$E_z=s_\alpha(1-s_p)i\frac{k}{\beta}J_m(k\rho)f_{ml}(\phi),$$

where $s_p=\pm 1$ for TE and TM modes, respectively, and $s_\alpha=\pm 1$ for forward and backward waves. The mode radial dependence is described in terms of Bessel functions of the first kind, J_m, and of their derivatives with respect to the argument, J_m'. The azimuthal variation is instead described by the functions g_{ml} and f_{ml} of the form

$$f_{ml}(\phi)=\begin{cases}\cos(m\phi) & l=\text{even}\\ \sin(m\phi) & l=\text{odd},\end{cases}$$
$$g_{ml}(\phi)=\begin{cases}-\sin(m\phi) & l=\text{even}\\ \cos(m\phi) & l=\text{odd}.\end{cases} \tag{A2}$$

The z component of the electric field is nonzero in the case of TM modes; it depends on k and is therefore very small.

The mode basis is orthonormal in the following sense:

$$\int dS\left[\frac{1}{Z^{p}}\mathbf{E}^{\alpha}_{kmpl}\mathbf{E}^{\alpha'}_{k'm'p'l'}+\frac{1}{Z^{p'}}\mathbf{E}^{\alpha}_{kmpl}\mathbf{E}^{\alpha'}_{k'm'p'l'}\right]=C^{\alpha}_{kmpl}\delta(k-k')\,\delta_{mm'}\,\delta_{pp'}\,\delta_{ll'}\,, \tag{A3}$$

where the modal impedance is defined as

$$Z^{p}=\sqrt{\frac{\mu_0}{\epsilon}}\times\begin{cases}\dfrac{K}{\beta}, & p=\text{TE mode}\\[2mm] \dfrac{\beta}{k}, & p=\text{TM mode}\end{cases} \tag{A4}$$

and $\epsilon=\epsilon_0 n_r^2$. The power normalization constant C^{α}_{kmpl} is

$$C^{\alpha}_{kmpl}=s_{\alpha}(Z^{p})^{-1}\frac{8\pi n_m}{k}, \tag{A5}$$

where

$$n_m=\begin{cases}2, & m=0\\ 1, & m\neq 0.\end{cases} \tag{A6}$$

The coupling coefficients are computed by explicitly introducing the expressions of the mode distributions (A1) in the definition (5). Recalling the characteristic relations of Bessel functions,

$$J_m(z)=\frac{z}{2m}[J_{m-1}(z)+J_{m+1}(z)],$$
$$J'_m(z)=\tfrac{1}{2}[J_{m-1}(z)-J_{m+1}(z)], \tag{A7}$$

and inserting Eq. (A7) in Eq. (5), one obtains

$$\begin{aligned}(K_t^{ff})_{\mu\mu'}=-\frac{i\omega}{C_\mu}\Delta\epsilon\frac{1}{4}\Bigg\{&\int_0^{2\pi}d\phi\, f_{ml}f_{m'l'}\\ &\times\int_0^{\rho(\phi)}\rho\, d\rho(s_pJ_{m_+}+J_{m_-})(s_{p'}J_{m'_+}+J_{m'_-})\\ &+\int_0^{2\pi}d\phi\, g_{ml}g_{m'l'}\int_0^{\rho(\phi)}\rho\, d\rho(J_{m_-}-s_pJ_{m_+})\\ &\times(J_{m'_-}-s_{p'}J_{m'_+})\Bigg\},\end{aligned} \tag{A8}$$

where the compact notations $J_{m\pm}=J_{m\pm1}(k\rho)$ and $J_{m'_\pm}=J_{m'\pm1}(k'\rho)$ have been introduced. In expression (A8) $\rho(\phi)$ represents the surface where a step discontinuity of the dielectric constant introduces the perturbation in the layer under analysis. In the case of elliptical geometries

$$\rho(\phi)=a\sqrt{\frac{1+\tan^2(\phi)}{1+\tan^2(\phi)\left(\dfrac{a}{b}\right)^2}} \tag{A9}$$

where a and b are, respectively, the major and minor axes of the ellipse and the angle ϕ taken with reference to the minor axis. In order to get more insight in expression (A8) and reduce the complexity of the numerical computations, it is convenient to invert the order in which the integrals over the radial and angular variable are performed. In the particular case of the ellipse, for example, where ρ is a periodic function of ϕ with period π, we obtain

$$\int_0^{2\pi}d\phi\int_0^{\rho(\phi)}\rho\, d\rho=\int_0^{b}\rho\, d\rho\sum_{n=0}^{1}\int_{n\pi+\bar{\phi}(\rho)}^{(n+1)\pi-\bar{\phi}(\rho)}d\phi. \tag{A10}$$

The extreme of integration, $\bar{\phi}(\rho)$, is obtained by inversion of the relation $\rho(\phi)$ (A9) on the angular interval $[0,\pi/2]$,

$$\bar{\phi}(\rho)=\begin{cases}0, & \rho<a\\ \tan^{-1}\left(\sqrt{\dfrac{1-(\rho/a)^2}{(\rho/b)^2-1}}\right), & a<\rho<b.\end{cases} \tag{A11}$$

The integral over the angular variable ϕ which appears in Eq. (A8) can be analytically performed and is of the form

$$\sum_{n=0}^{1}\int_{n\pi+\bar{\phi}(\rho)}^{(n+1)\pi-\bar{\phi}(\rho)}f_{ml}(\phi)f_{m'l'}(\phi)d\phi=[\psi_{m-m'}(\rho)+s_l\psi_{m+m'}(\rho)]\delta_{ll'}\,, \tag{A12}$$

where

$$\psi_{m\pm m'}(\rho)=\int_{\bar{\phi}(\rho)}^{\pi-\bar{\phi}(\rho)}\cos[(m\pm m')\phi]d\phi \tag{A13}$$

and

$$s_l=\begin{cases}1, & l=\text{even}\\ -1, & l=\text{odd}.\end{cases} \tag{A14}$$

The other contribution in Eq. (A8), obtained by performing the angular integration on the function $g_{ml}g_{m'l'}$, is very similar: on the basis of definition (A2), it differs from Eq. (A12) only for a change of sign in s_l. It is clear that Eq. (A13) is different from zero only when $m\pm m'$ is an even number, that is, the system couples only the modes with same azimuthal parity. Moreover, the term $\delta_{ll'}$ indicates that the modes with opposite polarization are completely uncoupled by the system: the odd angular dependence of the kind $\cos(m\phi)\sin(m'\phi)$, which would derive from $l\neq l'$, gives rise in Eq. (A12) to a vanishing contribution. These features, which stem from the even periodicity of the geometry under analysis, reduce the numerical complexity of the problem allowing us to solve separate eigenvalue problems, each of lower order. The rectangular and elliptical structures obviously fulfill these conditions, which are, however, far more general and include other different aperture shapes.

In conclusion, inserting expressions (A12) in Eq. (A8), the K_t^{ff} matrix elements reduce to integrals in the radial variable and are of the form

$$(K_t^{ff})_{\mu\mu'} = -\frac{i\omega}{C_\mu}\Delta\epsilon\frac{1}{2}\delta_{ll'}\int_0^b \rho\, d\rho\{\psi_{m-m'}(\rho) \times[J_{m'_-}J_{m_-}+s_p s_{p'}J_{m'_+}J_{m_+}]+s_l\psi_{m+m'}(\rho) \times[s_pJ_{m'_-}J_{m_+}+s_{p'}J_{m'_+}J_{m_-}]\}. \tag{A15}$$

The integral in the radial component must at this point be numerically evaluated. Only in the limit case of circular apertures, in which ψ is a constant function of ρ, the integral can be performed analytically.

In the case of the LP approximation (see Sec. II E) the mode normalization constant is found to be the same as Eq. (A5), while the K_t^{ff} matrix elements are now of the simpler form

$$(K_t^{ff})_{\mu\mu'} = -\frac{i\omega}{C_\mu}\Delta\epsilon\delta_{ll'}\int_0^{\rho_M} \rho\, d\rho[\psi_{m+m'}(\rho) + s_l\psi_{m-m'}(\rho)]J_m(k\rho)J_{m'}(k'\rho). \tag{A16}$$

[1] K. D. Choquette, R. P. Schneider, K. Lear, and K. Geib, Electron. Lett. **30**, 2043 (1994).

[2] C. Jung, R. Jäger, M. Grabherr, P. Schnitzer, R. Michalzik, B. Weigl, S. Müller, and K. J. Ebeling, Electron. Lett. **33**, 1790 (1997).

[3] G. R. Hadley, Opt. Lett. **20**, 13 (1995); **20**, 1483 (1995).

[4] Y-Z. Huang, J. Appl. Phys. **83**, 3769 (1998).

[5] G. R. Hadley, J. Lightwave Technol. **16**, 142 (1998).

[6] M. San Miguel, Q. Feng, and J. V. Moloney, Phys. Rev. A **52**, 2 (1995); **52**, 1728 (1995).

[7] G. Vershafelt, M. vander Vleuten, M. Creusenm, E. Smalbrugge, T. G. van de Roer, F. Karouta, R. C. Strijbos, J. Dankaert, I. Veretennicoff, B. Ryvkin, H. Thiepont, and G. A. Acket, IEEE Photonics Technol. Lett. **12**, 945 (2000).

[8] A. Valle, K. A. Shore, and L. Pesquera, J. Lightwave Technol. **14**, 2062 (1996).

[9] G. Giacomelli, F. Marin, M. Gabrysch, K. H. Gulden, and M. Moser, Opt. Commun. **146**, 136 (1998).

[10] M. P. van Exter, R. F. M. Hendriks, and J. P. Woerdman, Phys. Rev. A **57**, 2080 (1998).

[11] S. Balle, E. Tolkachova, M. San Miguel, J. R. Tredicce, J. Martin-Regalado, and A. Gahl, Opt. Lett. **24**, 1121 (1999).

[12] B. Ryvkin, K. Panajotov, A. Georgievski, J. Danckaert, M. Peeters, G. Verschaffelt, H. Thienpont, and I. Veretennicoff, J. Opt. Soc. Am. A **16**, 2106 (1999).

[13] M. Creusenm, G. Vershafelt, E. Smalbrugge, T. G. van de Roer, F. Karouta, I. Veretennicoff, H. Thiepont, and G. A. Acket, *1998 IEEE/LEOS Symposium, Benelux Chapter Proceedings, University of Gent, Gent, 1998* (University of Gent, Gent, 1998).

[14] C. Degen, B. Krauskopf, G. Jennemann, I. Fischer, and W. Elsäßer, J. Opt. B: Quantum Semiclassical Opt. **2**, 517 (2000).

[15] L. Fratta, P. Debernardi, G. P. Bava, C. Degen, J. Kaiser, I. Fischer, and W. Elsäßer (unpublished).

[16] A. V. Nesterov and V. G. Niziev, J. Phys. D: Appl. Phys. **33**, 1817 (2000).

[17] M. J. Noble, J. A. Lott, and J. P. Loehr, IEEE J. Quantum Electron. **34**, 2327 (1998).

[18] M. J. Noble, J. P. Loehr, and J. A. Lott, IEEE J. Quantum Electron. **34**, 1890 (1998).

[19] G. Liu, J.-F. Seurin, S. L. Chuang, D. I. Babic, S. W. Corzine, M. Tan, D. C. Barnes, and T. N. Tiouririne, Appl. Phys. Lett. **73**, 726 (1998).

[20] D. Burak and R. Binder, IEEE J. Quantum Electron. **33**, 1205 (1997).

[21] R. Kuszelewicz and G. Aubert, J. Opt. Soc. Am. A **14**, 3263 (1997).

[22] Q. Deng and D. G. Deppe, IEEE J. Quantum Electron. **33**, 2319 (1997).

[23] B. Demeulenaere, P. Bienstman, B. Dhoedt, and R. G. Baets, IEEE J. Quantum Electron. **35**, 358 (1999).

[24] P. Bienstman, B. Demeulenaere, B. Dhoedt, and R. G. Baets, J. Opt. Soc. Am. B **16**, 2055 (1999).

[25] A. W. Snyder and J. D. Love, *Optical Waveguide Theory* (Chapman & Hall, London, 1983).

[26] D. Marcuse, *Theory of Dielectrical Waveguides* (Academic Press, Boston, 1974).

[27] D. Marcuse, Bell Syst. Tech. J. **54**, 985 (1975).

[28] COST268 modeling exercise (http://www.ele.kth.se/cost268/WG1/WGExercizel.html), based on R. Kuszelewicz, CNET, Paris.

[29] P. Debernardi, A. Pisoni, and G. P. Bava, IEEE J. Quantum Electron. **30**, 93 (1994).

[30] M. Asada, IEEE J. Quantum Electron. **25**, 2019 (1989).

[31] K. D. Choquette and R. Leibenguth, IEEE Photonics Technol. Lett. **6**, 40 (1994).

[32] A. K. Jansen van Doorn, M. P. van Exter, and J. P. Woerdman, IEEE J. Quantum Electron. **34**, 700 (1998).

[33] M. P. van Exter, A. K. Jansen van Doorn, and J. P. Woerdman, Phys. Rev. A **56**, 845 (1997).